NASA Technical Memorandum 103105

Performance of a Supercharged Direct-Injection Stratified-Charge Rotary Combustion Engine

Timothy A. Bartrand
Sverdrup Technology, Inc.
Lewis Research Center Group
Brook Park, Ohio

and

Edward A. Willis
National Aeronautics and Space Administration
Lewis Research Center
Cleveland, Ohio

Prepared for the
Joint Symposium on General Aviation Systems
cosponsored by the AIAA and FAA
Ocean City, New Jersey, April 11–12, 1990

NASA

PERFORMANCE OF A SUPERCHARGED DIRECT-INJECTION STRATIFIED-CHARGE ROTARY COMBUSTION ENGINE

Timothy A. Bartrand
Sverdrup Tech. Inc., LeRC Group
2001 Aerospace Parkway
Brook Park, Ohio 44142

Edward A. Willis
Propulsion Systems Division
NASA Lewis Research Center
Cleveland, Ohio 44135

ABSTRACT

A zero-dimensional thermodynamic performance computer model for direct-injection stratified-charge rotary combustion engines was modified and run for a single rotor supercharged engine. Operating conditions for the computer runs were a single boost pressure and a matrix of speeds, loads and engine materials. A representative engine map is presented showing the predicted range of efficient operation. After discussion of the engine map, a number of engine features are analyzed individually. These features are: heat transfer and the influence insulating materials have on engine performance and exhaust energy; intake manifold pressure oscillations and interactions with the combustion chamber; and performance losses and seal friction. Finally, code running times and convergence data are presented.

INTRODUCTION

A brief list of the features that make a rotary combustion engine (RCE) a strong candidate as a small aircraft engine would include its large power-to-weight ratio, its ability to be configured into an engine package of small frontal area, its porting simplicity and its inherent balance (1)*. In addition, a direct-injection stratified-charge (DISC) RCE offers the advantages of greater fuel flexibility and improved fuel economy (2). Because of these advantages, research on DISC RCE improvement is ongoing at NASA, in industry and at the university level. As reported in the literature, a DISC RCE has run effectively on gasoline, jet fuel, diesel fuel and methanol (3). Currently, brake specific fuel consumptions (bsfcs) of 243–255 g/kW-hr (0.40–0.42 lb/hp-hr) at take-off and 231–249 g/kW-hr (0.38-0.41 lb/hp-hr) at cruise are indicated for an engine with a cruise power of 225 kW (300 hp) (4). These values for bsfc place the DISC RCE well within or under the fuel consumption of horizontally opposed, air cooled conventional piston aircraft engines in a similar power class (5).

In early carbureted RCEs, the positive features mentioned above were offset partially by a number of performance-degrading engine features. Gas seal leakage contributed to reductions in maximum torque, increases in bsfc and increases in hydrocarbon emissions (6). Flame quenching and crevice flows resulted in lost fuel energy and also contributed to bsfc and hydrocarbon emissions increases (7). Finally, slow combustion in the lagging part of the combustion chamber resulted in performance loss and higher emissions (8).

Harder, multi-section apex seals are considered by many to have solved engine sealing problems

* Numbers in parentheses designate references at the end of the paper.

(3). Because the performance of Wankel engines has been improved, it is reasonable to assume the sealing problem has been diminished, although direct measurements of leakage flows in firing engines are difficult to perform. Combustion-related problems have been addressed through the use of dual spark plugs and fuel injection. Suggestions for further improvement of rotary engine performance include insulation of engine components (9), use of improved fuel injection patterns and optimization of rotor pocket and port designs. Fuel injector improvements have been made possible to a large extent through the use of multi-dimensional engine modelling of flow in the combustion chamber (10).

PURPOSE

This report summarizes the results of a computer program written to analyze the performance of a state-of-the-art DISC RCE. A zero-dimensional thermodynamic engine cycle computer model has generated performance data for a single rotor DISC RCE. This satisfied two goals: to map the performance of a hypothetical state-of-the-art RCE and to exercise a modified engine analysis program. In the current study, the intent was not to predict the performance of a specific engine, but to show the general features of DISC RCE performance and to demonstrate the capabilities of an updated computer program.

BACKGROUND

The computer code used in this study (referred to as the MIT code) was initially developed at MIT under the direction of Dr. John Heywood. The first rotary engine code was derived from an existing crank-piston engine thermodynamic model. It predicted the performance of a carbureted RCE (11). The carbureted Wankel model employed a Wiebe function for estimation of burning rate and included crevice/leakage effects. Constant wall temperatures were used and manifold thermodynamic properties were fixed. In its next stage of development at MIT, a DISC combustion heat release model was added. The heat release rate model is described in reference (12). The most complete reference describing the DISC MIT code is the masters thesis presented by Roberts (13). Nguyen et al. applied Roberts' version of the MIT code to a DISC RCE designed by the Outboard Marine Corporation and run at NASA Lewis Research Center (14). Results of a comparable thermodynamic computer model were published by Dimplefeld (15), along with comparisons with engine data. The final development of the MIT code at MIT was performed by Stanten (16), who added the provision for user-defined trochoid housing surface temperatures.

At NASA Lewis Research Center, in addition to funding experimental and industry development of the DISC RCE, computer programs are being written and modified to gain insights into engine performance and in-cylinder processes. Multi-dimensional computer programs under development include those of Raju (17) and Shih et al. (18). In thermodynamic modelling, the MIT DISC engine code has been modified; the modified version was used to produce the results in this paper. A number of major changes have been made to the MIT code at NASA. First, steady state heat transfer models for the rotor face, side housings, trochoid housing and exhaust pipe were added. Also, intake manifold pressure, temperature and mass are now allowed to vary during the intake process. Accounting of crevice mass accumulation was changed, as well as the convergence process and the selection of cycle initial conditions. Finally, kinematic models for seal and bearing friction were added, along with an ad hoc model for estimating losses associated with ancillary components. In the following section of this paper, the basic governing equations of the MIT code will be reviewed briefly and the additions will be described in greater detail.

Due to the MIT code's much shorter computational time, it has many capabilities and can address engine development questions that are not addressed by the multi-dimensional codes mentioned above. On the negative side, the code relies on empirical constants. If experimental data are not

first obtained for an engine, the MIT code can only demonstrate trends. Nonetheless, such a model as the MIT code is useful in preliminary investigations of engine configurations and may be used as part of a larger turbocharged/turbocompounded engine simulation.

MODEL FORMULATION AND CALIBRATION

A brief overview of the original DISC MIT code governing equations is presented in this section, along with a more detailed treatment of the additions made to the code at NASA. For more detailed information, the reader is directed to references (11), (13) and (16).

The MIT code follows the progress of one of the three RCE combustion chambers through a number of engine cycles until steady operation is achieved. The gas in the combustion chamber and in the manifolds is considered well mixed.

Figure 1 is a schematic of a RCE. The indicated chamber is in the minimum volume, top dead center (TDC) position. In the MIT code, this position is designated as crank angle, θ, equal to 0°. The engine cycle begins as the intake port opens (when the lead apex seal begins to uncover the intake port) at crank angle θ_{ipo} and lasts for one rotor revolution. Since the rotor rotates at 1/3 the rate of the crankshaft, one cycle lasts $3 \times 360° = 1080°$. θ_{ipc}, θ_{sp}, θ_{epo} and θ_{epc} are crank angles for intake port closing, spark firing, exhaust port opening and exhaust port closing, respectively. For the above definition of crank angle, θ_{ipo}, θ_{ipc} and θ_{sp} are negative while θ_{epo} and θ_{epc} are positive. The MIT code is considered converged when the chamber pressure, P_c, the chamber temperature, T_c, the chamber mass, m_c, the intake manifold pressure, P_{im} and the rotor and housing temperatures vary less than a user-input tolerance between engine cycles.

As the code marches in crank angle, the derivatives of chamber temperature, pressure, mass and composition are calculated and integrated. In addition, leakage flow rates, heat transfer rates and rate of change of manifold properties are calculated on a crank angle by crank angle basis. Chamber pressure, temperature, mass and composition are governed by the conservation of mass, species and energy and the ideal gas relation. Thermodynamic properties are calculated using approximate, empirical relations for hydrocarbon-air combustion products (19). Flow rates into and out of the chamber, including intake, exhaust and leakage through gas seals, are quasi-steady, 1-D compressible; the mass flow rate is uniquely determined by upstream temperature, pressure and composition, downstream pressure and user-input discharge coefficient. Port areas and leakage area per chamber are also input. Backflow of chamber contents into the intake manifold is allowed.

Combustion proceeds according to an input empirical heat release rate. As shown in Figure 2, heat release takes place in two phases. First, there is a linear rise to the maximum heat release rate:

$$\frac{dQ}{d\theta} = \left(\frac{dQ}{d\theta}\right)_{max} \left(\frac{\theta - \theta_{sp}}{\theta_{qmax} - \theta_{sp}}\right) \tag{1}$$

where $\frac{dQ}{d\theta}$ is the rate of fuel energy heat release per crank angle degree, $\left(\frac{dQ}{d\theta}\right)_{max}$ is the maximum heat release rate encountered and θ_{qmax} is the crank angle for the maximum heat release rate. After the linear rise, the heat release rate falls exponentially according to

$$\frac{dQ}{d\theta} = \left(\frac{dQ}{d\theta}\right)_{max} \exp\left\{\frac{-(\theta - \theta_{qmax})}{\tau}\right\} \tag{2}$$

Inputs to the MIT code combustion model are $\left(\frac{dQ}{d\theta}\right)_{max}$ and θ_{max}. τ is calculated assuming complete combustion of fuel. Ideally, a set of combustion model inputs would be provided to the code for various engine speeds and loads, depending on the variation of the combustion process

with speed and load. In the absence of engine pressure data to derive these combustion model inputs, the same values were used for all operating conditions in this study. The values used for these constants were chosen based on the authors' experience and the work of Nguyen (14). Using the same combustion model inputs for all engine operating conditions is expected to result in error, especially at high engine speeds when the time for all the fuel to burn becomes a greater fraction of the time to complete one engine cycle for an actual engine.

Heat transfer coefficient between the chamber gas and the trochoid housing inner surface, the rotor face and the side housing surfaces is calculated according to

$$Nu = \beta Re^{\alpha} \; Pr^{\gamma} \tag{3}$$

where Nu is Nusselt number based on the chamber depth, Re is Reynolds number based on chamber depth, Pr is Prandtl number and β, g and h are empirical constants. This relation was proposed by Woschni (20). During intake, compression and exhaust, the velocity used in the Reynolds number is the rotor tip speed. During combustion, another term is added to velocity to include combustion turbulence effects. For the results presented, the constants in equation 3 were $\beta = 0.038$, $g = 0.8$ and $h = 1$. An attempt was made to implement an alternative relation proposed by Lee and Schock (21), but this relation did not produce acceptable qualitative results; the peak heat transfer rates did not occur at or near TDC.

Steady state wall temperature calculations are now made in the MIT code. The trochoid housing is divided into 30 segments. The midpoints of these segments are shown in Figure 3. A steady state wall temperature calculation is made at each segment's midpoint. The trochoid housing can be made of up to three materials, each with its own thickness and thermal conductivity. The hot gas side heat transfer coefficient at the segment midpoints is taken as the average of the heat transfer coefficient (equation 3) over the 360° surrounding the segment. The coolant side heat transfer coefficient is calculated internally with user-input coolant properties and flow rate and allowing for nucleate boiling. As can be seen from the thermal resistance schematic in Figure 4, the wall temperature, T_{wall} is

$$T_{wall} = \frac{\overline{h_{hg}}\;\overline{T_c} + UT_{cool}}{U + \overline{h_{hg}}} \tag{4}$$

where $\overline{h_{hg}}$ is average hot gas heat transfer coefficient, $\overline{T_c}$ is average chamber temperature and U is overall heat transfer coefficient from the inner housing surface to the coolant. For the housing cross section shown in Figure 4,

$$U = \frac{1}{L_1/k_1 + L_2/k_2 + L_3/k_3 + 1/h_{cool}} \tag{5}$$

where L_1, L_2 and L_3 are thicknesses of materials 1, 2, and 3, k_1, k_2 and k_3 are thermal conductivities of materials 1, 2 and 3 and h_{cool} is the coolant side convective and boiling heat transfer coefficient. Equation 5 assumes housing curvature effects are small.

A steady state heat transfer model applied at each segment midpoint is the most practical for use with a thermodynamic model. A similar approach was used by Assanis and Badillo (22) and produced adequate results for metal engines, but less satisfactory results for insulated engines. It is likely that errors in using a steady state heat transfer model will be less for the trochoid housing, since each housing position "sees" only a limited part of the cycle and is therefore subject to less severe swings in temperature. Another short-coming of the steady-state heat transfer model is its insensitivity to heat-transfer-driven changes in the combustion process. When wall temperature,

porosity and radiation characteristics are changed, the combustion process may also change. Unless the MIT code combustion model is recalibrated for each set of housing and rotor materials, changes in the combustion process will not be reflected in predicted performance.

Side plate temperatures are calculated similarly to trochoid housing temperatures, with the exception that the coolant side heat transfer coefficient is input and does not include nucleate boiling. The rotor face temperature also is calculated assuming one dimensional steady state heat transfer. The hot gas side heat transfer coefficient and gas temperature are set equal to the cycle averages and the heat transfer coefficient is a user-input value. The value used for rotor coolant heat transfer coefficient was estimated reflecting a "cocktail shaker" type oil flow in the rotor cavity.

Intake manifold thermodynamic properties including intake manifold pressure, P_{im}, temperature, T_{im}, and mass, m_{im}, can either be fixed or allowed to vary during the intake process. Intake manifold volume, V_{im}, does not change. For variable intake manifold properties, the first cycle of the run is made with fixed properties to estimate air mass flow rate to the manifold. For subsequent cycles, the air mass flow rate to the manifold is constant during the cycle and the rate of change of intake manifold mass, $\dot{m}_{im}$, is given by

$$\dot{m}_{im} = \dot{m}_{ic} - \dot{m}_{int} \tag{6}$$

where $\dot{m}_{ic}$ is mass flow rate into the intake manifold (e.g., from an aftercooler) and $\dot{m}_{int}$ is mass flow rate from the intake manifold to the combustion chamber. The derivative of intake manifold temperature is

$$\frac{dT_{im}}{dt} = \left(\frac{T_{im}}{P_{im}V_{im}}\right)\left(\frac{\dot{m}_{ic}(i_{ic} - i_{im}) + \Re T_{im}\dot{m}_{im} + \dot{Q}_{im}}{c_{p,im}/\Re - 1}\right) \tag{7}$$

where i_{ic} is the enthalpy of the incoming stream, i_{im} is the enthalpy in the intake manifold, $\Re$ is the gas constant for air, $\dot{Q}_{im}$ is heat transfer rate to manifold walls (taken as zero for the current study) and $c_{p,im}$ is specific heat at constant pressure in the intake manifold. Pressure rate of change is

$$\frac{dP_{im}}{dt} = \left(\frac{\Re T_{im}}{V_{im}}\right)\dot{m}_{im} + \left(\frac{P_{im}}{T_{im}}\right)\frac{dT_{im}}{dt} \tag{8}$$

Apex seal friction force is calculated following the approach given by Yamamoto (23), but taking into consideration friction between the seal slot and the seal and also using pressures generated by the MIT code. For any crank angle, θ, calling the pressure ahead of the apex seal P_1 and that behind the seal P_2, the instantaneous apex seal friction force, F_{af}, is

$$F_{af} = \frac{\mu_a}{\cos\varphi}\left\{l_a\left(\frac{b_a}{2} + a_r\sin\varphi\right)(P_1 - P_2) + m_a\left(\frac{d\theta}{dt}\right)^2\left[\frac{r}{9} + \epsilon\cos\left(\frac{2\theta}{3}\right)\right] - \right.$$

$$\mu_a m_a\left(\frac{d\theta}{dt}\right)^2\sin\left(\frac{2\theta}{3}\right) - \mu_a P_1 l_a(h_a - c_a) -$$

$$\left.\mu_a l_a(P_1 - P_2)(c_a - a_r + a_r\cos\varphi) + F_{sa}\right\} \tag{9a}$$

when $P_1 > P_2$ or

$$F_{af} = \frac{\mu_a}{\cos\varphi}\left\{l_a\left(\frac{b_a}{2} + a_r\sin\varphi\right)(P_2 - P_1) + m_a\left(\frac{d\theta}{dt}\right)^2\left[\frac{r}{9} + \epsilon\cos\left(\frac{2\theta}{3}\right)\right] -\right.$$

$$\mu_a m_a \left(\frac{d\theta}{dt}\right)^2 \sin\left(\frac{2\theta}{3}\right) - \mu_a P_2 l_a (h_a - c_a) -$$

$$\mu_a l_a (P_2 - P_1)(c_a - a_r + a_r \cos\varphi) + F_{sa}\Big\} \tag{9b}$$

for $P_2 > P_1$. In equations 9a and 9b, μ_a is the apex seal's sliding coefficient of friction on the trochoid housing, b_a is the apex seal width, a_r is the radius of curvature for the apex seal crown, m_a is the apex seal mass, r is the rotor generating radius, ϵ is the engine eccentricity, c_a is the clearance between the rotor tip and the seal tip, l_a is the seal depth (equal to the chamber depth), F_{sa} is the spring force on the seal and φ is the seal lean angle, given by

$$\varphi = \arccos\left\{\frac{3\epsilon\cos[\frac{2}{3}(\theta + 180°)] + r}{\sqrt{9\epsilon^2 + r^2 + 6\epsilon r\cos[\frac{2}{3}(\theta + 180°)]}}\right\} \tag{10}$$

Side seal friction force is assumed lumped at the seal center. It arises due to both gas pressure loads and spring force. Side seal friction force, F_{sf}, is given by

$$F_{sf} = \mu_s F_{ss} + (b_s - \mu_s h_s)\mu_s l_s P_c \tag{11}$$

where μ_s is the coefficient of sliding friction for the side seal on the side housing, F_{ss} is the side seal spring force, b_s is the side seal width, h_s is the side seal height, l_s is the side seal length and P_c is the instantaneous chamber pressure. The crank case pressure, P_{cc}, is assumed constant, so the oil seal friction force, F_{of} is given by

$$F_{of} = 2\pi R_o b_o \mu_o P_{cc} + \mu_o F_{so} \tag{12}$$

In equation 12, R_o is the oil seal radius, b_o is the oil seal width, μ_o is the oil seal sliding coefficient of friction and F_{so} is the oil seal spring force. At Michigan State University, modelling work for seal friction is currently underway. This work is expected to result in more sophisticated seal models for use in the MIT code (24).

Ancillary losses were lumped together and estimated in a manner similar to that of other intermittent combustion engine thermodynamic programs. Heywood (25) recommends a relation of the form

$$fmep = C_{F1} + C_{F2}\left(\frac{N}{1000}\right) + C_{F3}\left(\frac{N}{1000}\right)^2 \tag{13}$$

for friction mean effective pressure ($fmep$) in a spark ignition engine. Here, C_{F1}, C_{F2} and C_{F3} are constants and N is engine speed in rpm. The first term is associated with boundary lubrication, the second term with hydrodynamically lubricated surfaces in relative motion and the third with fluid losses (air, water, fuel and oil pumping). Because the MIT code calculates the seal and bearing friction loads separately, equation 13 was modified to

$$fmep_a = C_{A1} + C_{A2}\left(\frac{N}{1000}\right)^2 \tag{14}$$

where $fmep_a$ is the ancillary $fmep$ and C_{A1} and C_{A2} are constants. The only available data for use in calibrating equation 14 were unpublished data (26). Using these data, the constants in equation 14 were set to $C_{A1} = 0.45$ and $C_{A2} = 0.025$.

RESULTS

The MIT code was run for a single rotor engine in the 75 kW class for engine speeds ranging from 3500 to 8500 rpm and for fuel/air equivalence ratios between 0.35 and 0.85. The engine was supercharged to an average boost pressure of 86.1 kPa (12.5 psig) and the exhaust manifold pressure was set at 152 kPa (22 psia). Fuel used was iso-octane. The baseline engine had housings made of aluminum and a rotor made of iron. Engine coolant was a 50/50 mixture of water and ethylene glycol. There were two main bearings, two rotor bearings, three apex seals, six side seals and two oil seals. Leakage area was estimated at 0.1 cm^2 and crevice volumes at 0.57 cc. Discharge coefficients were 0.6 and 0.65 for the intake and exhaust ports, respectively.

PERFORMANCE

A P-V diagram was generated for a baseline engine (Figure 5). Although chamber properties, etc., are calculated at fractional crank angle steps, output was only generated for crank angle increments of 10°. The shape of the plot is expected, but three points should be noted. First, there is a small positive pumping loop (resulting in work added to the system), since the intake pressure is greater than the exhaust and chamber pressures during the scavenging process. Second, the peak chamber pressure location, 28° after TDC, and magnitude, 60.4 atm, are determined by inputs to the combustion model, which was not adjusted to reflect burning rate changes with speed and load. Finally, the peak chamber pressure is well above the critical pressure for *n*-octane, 24.8 atm (27). The thermodynamic cycle description is completed in Figure 6, which shows chamber temperature and the combustion progress for one cycle. Combustion progress is defined as the fraction of the total fuel for one cycle burnt by a given crank angle (0 means combustion has not begun, 1 means combustion is complete). As expected, the temperature drop is more gradual than the pressure drop during the expansion process.

The results of this study are summarized in Figure 7. The performance of a hypothetical DISC RCE is mapped over a domain of engine speeds and loads. Lines of constant equivalence ratio are plotted and contours of iso-bsfc are superimposed. Constant equivalence ratio lines flatten out with engine speed because of volumetric efficiency decreases. The high bsfcs seen at low load arise because the ancillary losses are such a large fraction of indicated power. The engine map shows a fairly large region of operating conditions for which fuel consumption is below 290 g/kW-hr (0.48 lb/hp-hr). Some cautions should be noted, however. First, this engine map was generated for only one boost pressure; to fully map engine performance, a family of these maps should first be generated and then "matched" to the characteristics of the turbocharger in use. Secondly, no attempt was made to optimize engine performance or fuel consumption. Finally, the performance may be worse than predicted at high speeds, because of injector and combustion changes. The engine map of Figure 7 was generated in approximately 1.5 hr CPU time on a VAX 11/780 mainframe computer.

HEAT TRANSFER

To investigate the ability of insulating coatings and materials to enhance engine performance and exhaust gas energy, the MIT code was run for six sets of engine materials: the baseline engine (aluminum housings and iron rotor), an all titanium engine, an engine with a ceramic coated trochoid housing, an engine with a ceramic coated rotor, an engine with all surfaces ceramic coated and a hypothetical, adiabatic engine. Because chamber pressure data were not available for calibration of the combustion model for each of these engines, the same combustion model inputs are used for all six engines. This may lead to inaccurate predictions should the wall temperatures or properties become very different from those of the baseline engine. The exact make-up and material properties of these engine components are detailed in Table 1. The coatings used were chosen to be the same as those of Badgley et al. (9).

Table 1: Engine Materials for the Six Heat Transfer Test Cases

Case	Trochoid Housing	Rotor Face	Side Housing
1	11.25mm Aluminum*	11.25mm Iron**	11.25mm Aluminum
2	10.76mm Titanium***	10.63mm Titanium	10.76mm Titanium
3	10mm Al coated with 0.127mm of coating 1† and 0.635mm of coating 2‡	11.25mm Iron	11.25mm Aluminum
4	11.25mm Aluminum	10mm Iron coated with 0.635mm of coating 2	11.25mm Aluminum
5	10mm Al coated with 0.127mm of coating 1 and 0.635mm of coating 2	10mm Iron coated with 0.635mm of coating 2	10mm Al coated with 0.127mm of coating 1 and 0.635mm of coating 2
6	Hypothetical Structure with near-zero conductivity	Hypothetical Structure with near-zero conductivity	Hypothetical Structure with near-zero conductivity

* For Aluminum, k=240 w/m-k
** For Iron, k=547 w/m-k
*** For Titanium, k=19.4 w/m-k
† Coating 1 is Plasma Sprayed Cr_2O_3, k=1.21 w/m-k
‡ Coating 2 is Plasma Sprayed Zirconia, Post Densified with Cr_2O_3, k=2.91 w/m-k

In Figure 8, predicted trochoid housing inner surface temperatures are plotted for 30 housing positions (see Figure 3 for the 30 positions). Because nucleate boiling was allowed on the coolant side of the housing, coolant heat transfer coefficients became very high when the trochoid housing temperature on the coolant side approached the liquid saturation temperature. The result is very little swing in housing temperature for the aluminum housings. Predicted peak temperature for the coated housing (T_{wall} = 672 K, [750°F]) was considerably below the prediction of Badgley et al. (T_{wall} = 991 K [1324°F]) for a liquid cooled engine of the same size category. In predicting their wall temperatures, Badgley et al. used the version of the MIT DISC engine code from MIT without the changes that were made subsequently at NASA. The MIT code was used to generate boundary conditions for a multi-dimensional, finite element steady state heat conduction analysis of the trochoid housing. Badgley's model is steady state, in that averaged chamber temperatures and heat transfer coefficients are used on the hot side of the housing walls. Coolant side heat transfer coefficient and temperature for the finite element analysis were chosen and fixed (apparently the same values for all housing positions). Two possible explanations are offered for the differences between predicted housing temperatures. First, coolant side heat transfer coefficient was determined differently in the two studies. Also, the analysis used in the present study is 1-D, whereas that of Badgley et al. was 3-D (although the boundary conditions were not time dependent). Neither calculation accounted for possible changes in the combustion process.

Also found on Figure 8 are predicted housing temperatures for an all-titanium engine and a hypothetical adiabatic engine. The predicted housing temperatures for all the engines shown in Figure 8 are well below those of a truly adiabatic engine.

Figure 9 illustrates the redistribution of fuel energy from the coolant to work and exhaust when the engine is insulated. In all cases but the adiabatic engine, only modest decreases in coolant load are realized. In general, most of the fuel energy diverted from the coolant appears in the exhaust stream, as demonstrated in the adiabatic engine case. Note that this analysis was performed at only one engine speed, 5500 rpm. At lower engine speeds, since heat transfer is time (and not crank angle) dependent, the fraction of the fuel energy lost to the coolant will be higher and the influence of insulating materials more pronounced. The effect insulating materials have on mean exhaust gas temperature, brake power and bsfc is shown in Table 2. Volumetric efficiency for the coated and titanium engines was nearly the same as that of the baseline engine (93 %). The volumetric efficiency of the hypothetical adiabatic engine was 91 %.

Table 2: Influence of Engine Materials on Performance

Case	% of Fuel Energy to Cooling (%)	$\overline{T}_{exh}$ (K)	Normalized Brake Power (-)	BSFC (g/kW-hr)
1	12.5	964.5	1.0	281
2	11.0	975.5	1.012	278
3	11.7	969.7	1.008	279
4	12.4	965.7	1.002	281
5	11.5	971.3	1.008	279
6	0	1064.6	1.06	260

In Figure 10, the breakdown of coolant heat transfer to the trochoid housing, the rotor face and the sideplates is shown. Since the percentage of heat transfer through the rotor and sideplates is small (in terms of fuel energy), it appears that insulating the trochoid housing would have a greater impact on exhaust gas energy. Because the apex seals scrape the trochoid surface, though, care must be taken in choosing a housing coating and applying it to the surface. Although weight was not analyzed in this study, it is suggested an added benefit of an insulated aircraft engine is its lower cooling system weight.

MANIFOLD PROPERTIES

Since MIT code results were last published, provisions for variable intake manifold pressure, temperature and mass have been added. The formulation is described in this report's Model Formulation and Calibration section. The instantaneous intake manifold pressures for an engine run with an equivalence ratio of 0.75 and engine speeds ranging from 3500 to 8500 rpm are shown in Figure 11. Although a relatively large manifold volume was used (equal to the engine displacement volume), the intake manifold pressure variation during one intake event is large, $\sim$ 30% of the average intake manifold pressure at 3500 rpm. The peak pressure decreases and shifts to later crank angles as engine speed is increased. Since peak pressures are high and early in the intake process (before

the exhaust port closes), there is significant blow-through of fresh air through the exhaust port at low speeds. In addition, since the pressure at the time the intake port closes is higher for low speeds, the volumetric efficiency also is expected to be higher. Volumetric efficiency was calculated based on average manifold pressure and temperature. No comparisons are made with empirical data, since no data were available. In the future, if a need is shown, a more complex, geometry dependent 1-D intake manifold model may be incorporated.

The MIT code was run for the same operating conditions and with both variable and fixed intake manifold thermodynamic properties. Intake manifold volume was not changed for any runs. Figure 12 shows a significant difference between predicted air flow rate and trapping efficiency for the fixed and variable property cases. Trapping efficiency is defined as the percentage of the air flowing through the intake port that is trapped in the chamber when the intake port closes. Both the air mass flow rate and the trapping efficiency are lower for the variable intake manifold thermodynamic property model than for the fixed property model.

In Figure 13, volumetric efficiency and brake power are plotted for the variable and fixed intake manifold property models. Because of the tuning effects described above, the volumetric efficiency of the variable manifold pressure engine is higher at low speeds and lower at high speeds compared to that of the fixed property engine. These volumetric efficiency differences also are reflected in the output power curves.

LOSSES

Figure 14a shows the estimated ancillary fmep, $fmep_a$, for an engine run at $\phi = 75$. Recalling equation 14, $fmep_a$ rises with the square of engine speed. Note that $fmep_a$ has no load dependency. The $fmep_a$ includes contributions from the water pump, the oil pump, the fuel pump, the alternator and the acceleration of oil in the rotor cavity.

In Figure 14b, seal friction losses for the same engine and a motored engine are plotted against engine speed. The seal $fmep$ is lower than $fmep_a$. The relatively small influence of equivalence ratio on friction is demonstrated in Figure 14b. Since crank case pressure is not varied, the oil seal friction losses are the same for the motored and the fired engine. Because apex seal losses are dominated by the centrifugal force exerted on the seal, not by gas pressure, apex seal losses are predominantly influenced by engine speed. The side seals show a greater sensitivity to gas pressure, because they have a greater base area (there are six side seals) and are subjected to the chamber pressure.

Friction mean effective pressure is plotted against engine speed for three equivalence ratios in Figure 15. $fmep$ in Figure 15 includes seal friction, bearing friction and ancillary losses. A more revealing comparison of the friction losses at different engine loads is made in Figure 16, where the fraction of the indicated power used to overcome friction losses is plotted against engine speed for 3 equivalence ratios. At low loads, the friction consumes a greater fraction of the engine indicated power. This results in the high bsfcs at low loads shown on the engine map (Figure 7).

CODE STATISTICS

Table 3 shows convergence data and CPU times for a number of runs. Normally the MIT code requires between 3 and 12 engine cycles to converge for one set of engine operating conditions. This equates to between 1 and 3 CPU minutes to run on a VAX 11/780 mainframe computer.

Table 3: Computer Program Statistics

Case	Cycles to Converge	$(\Delta P_c)_{initial}$	$(\Delta T_c)_{initial}$	$(\Delta P_{im})_{initial}$	CPU Time (min)*
ϕ=0.75, 3500 rpm	6	0.02%	-0.42%	0.05%	1:42
ϕ=0.75, 5500 rpm	5	0.05%	-0.16%	0.71%	1:24
ϕ=075, 7500 rpm	7	0.10%	-0.08%	0.26%	1:54
Motored, 7500 rpm	6	0.04%	-0.13%	0.86%	1:45
Motored, 7500 rpm, P_{im} = constant	4	0.06%	-0.06%	0.00%	1:03

* On a VAX 11/780 Mainframe Computer

CONCLUSIONS

A hypothetical, one rotor DISC RCE was analyzed with a zero-dimensional thermodynamic engine cycle computer program. The program predicted a broad range of operating conditions over which the engine could run at desired power for fuel consumption below 290 g/kW-hr (0.48 lb/hp-hr). Insulating the engine with a thin coating of ceramic material resulted in small reductions in the coolant load and very small improvements in performance. It is possible the steady state approach used to calculate heat transfer resulted in underprediction of the positive effects of insulation. In addition, it was assumed changes in wall temperature and wall material properties did not have a large influence on the combustion heat-release rate.

A new intake manifold model was demonstrated. There are significant differences in predicted air mass flow rate and volumetric efficiency when the intake manifold properties are allowed to vary, as opposed to using a fixed intake pressure and temperature. There is a significant variation in pressure in the intake manifold during the intake process.

Engine losses were estimated using kinematic models for all seals and bearings, and using an ad hoc model to estimate all other ancillary losses. In general, losses are more influenced by engine speed than load. It would be desirable to incorporate separate models for the ancillary components such as water pump, fuel pump, oil pump and alternator.

When engine pressure data become available for a DISC RCE for a number of loads and speeds, a set of combustion model inputs for the MIT code will be calculated. The domain over which a set of combustion rate model inputs is valid will be determined with these values. Until that time, the MIT code can only be used to make qualitative studies on engine performance. Other model constants that need to be calibrated include friction and heat transfer model inputs.

The MIT code is an inexpensive tool for analyzing DISC Wankel engines. It normally runs in less than 3 min on a VAX 11/780 computer and produces information for a wide range of engine performance indicators. It has been shown to be flexible enough to incorporate submodels for friction and other engine processes and it appears compatible for use in a turbocharged/turbocomponded engine system analysis.

REFERENCES

(1) Jones, C.,"The Curtiss-Wright Rotating Combustion Engines Today," Paper 886D, SAE Transactions, pp.127-147, 1965.

(2) Willis, E. A. and Wintucky, W. T.,"An Overview of NASA Intermittent Combustion Engine Research," Paper AIAA-84-1393, AIAA/SAE/ASME Joint Propulsion Conference, Cincinnati, Ohio, 1984.

(3) Jones, C., "An Update of Applicable Automotive Engine Rotary Stratified Charge Developments," SAE Paper 820347, International Congress and Exposition, Detroit, Michigan, 1982.

(4) Mount, R. E. and LaBouff, G. A., "Advanced Stratified Charge Rotary Engine Design," SAE Paper 890324, International Congress and Exposition, Detroit, Michigan, 1989.

(5) McCormick, B. W., Aerodynamics, Aeronautics and Flight Mechanics, p. 338, John Wiley & Sons, New York, 1979.

(6) Eberle, M. K. and Klomp, E. D., "An Evaluation of Potential Performance Gain from Leakage Reduction in Rotary Engines," SAE Paper 730117, International Automotive Engineering Congress, Detroit, Michigan, 1973.

(7) Danieli, G. A., Ferguson, C. R., Heywood, J. B. and Keck, J. C., "Predicting the Emissions and Performance Characteristics of a Wankel Engine," SAE Paper 740186, International Automotive Engineering Congress, Detroit, MI, 1974.

(8) Ferguson, C. R., Danieli, G. A., Heywood, J. B. and Keck, J. C., "Time Resolved Measurements of Exhaust Composition and Flow Rate in a Wankel Engine," SAE Paper 750024, International Automotive Engineering Congress and Exposition, Detroit, MI, 1975.

(9) Badgley, P. R., Doup, D. and Kamo, R., "Analysis and Test of Insulating Components for Rotary Engine," SAE paper 890326, International Automotive Engineering Congress and Exposition, Detroit, Michigan, 1989.

(10) Abraham, J., Wey, M.-J. and Bracco, F. V., "Pressure Non-Uniformity and Mixing Characteristics in Stratified-Charge Rotary Engine Combustion," SAE paper 880624, International Automotive Engineering Congress and Exposition, Detroit, Michigan, 1988.

(11) Norman, T. J., A Performance Model of a Spark Ignition Wankel Engine: Including the Effects of Crevice Volumes, Gas Leakage and Heat Transfer, Masters Thesis, Massachusetts Institute of Technology, June, 1983.

(12) Gatowski, J. A., Balles, E. N., Chun, K. M., Nelson, F. E., Ekchian, J. A. and Heywood, J. B., "Heat Release Analysis of Engine Pressure Data," SAE paper 841359, Fuels and Lubricants Meeting and Exposition, Baltimore, Maryland, 1984.

(13) Roberts, J. M., Heat Release Estimation and Prediction of Wankel Stratified-Charge Combustion Engine, Masters thesis, Massachusetts Institute of Technology, September, 1985.

(14) Nguyen, H. L., Addy, H. E., Bond, T. H., Lee, C. L. and Chun, K. S.,"Performance and Efficiency Evaluation and Heat Release Study of a Direct-Injection Stratified-Charge Rotary Engine," SAE paper 870445, International Automotive Engineering Congress and Exposition, Detroit, Michigan, 1987.

(15) Dimplefeld, P. and Humke, A.,"Heat Release Characteristics of Stratified-Charge Rotary Engines," SAE paper 870443, International Automotive Engineering Congress and Exposition, Detroit, Michigan, 1987.

(16) Stanten, R. A., Heat Transfer and Performance Calculations in a Rotary Engine, Masters thesis, Massachusetts Institute of Technology, August, 1987.

(17) Raju, M. S.,"Analysis of Rotary Engine Combustion Processes Based on Unsteady, Three-Dimensional Computations," paper AIAA-90-0643, AIAA 28th Aerospace Sciences Meeting, Reno, Nevada, 1990.

(18) Li, Z., Shih, T. I-P. and Nguyen, H. L., "Modelling and Simulation of Wankel Engine Flow Fields," SAE paper 900029, International Automotive Engineering Congress and Exposition, Detroit, Michigan, 1990.

(19) Martin, M. K. and Heywood, J. B,"Approximate Relationships for the Thermodynamic Properties of Hydrocarbon-Air Combustion Products," Vol. 15, pp. 1–10, Combustion Science and Technology, Gordon and Breach Science Publishers Ltd., Gr. Britain, 1977.

(20) Woschni, G.,"A Universally Applicable Equation for the Instantaneous Heat Transfer Coefficient in the Internal Combustion Engine," SAE paper 670931, 1967.

(21) Lee, C. M. and Schock, H. J.,"Regressed Relations for Forced Convection Heat Transfer in a Direct Injection Stratified Charge Rotary Combustion Engine," NASA Technical Memorandum 100124, 1988.

(22) Assanis, D. N. and Badillo, E.,"Transient Conduction in Low-Heat-Rejection Engine Combustion Chambers," SAE paper 870156, Automotive Engineering International Congress and Exposition, Detroit, Michigan, 1987.

(23) Yamamoto, K., Rotary Engine, Toyo Kogyo Co., Ltd., Hiroshima, Japan, 1969.

(24) Rachel, T. and Schock, H. J., Personal communication, Michigan St. Univ., Dept. of Mech. Engr., December, 1989.

(25) Heywood, J. B., Internal Combustion Engine Fundamentals, p. 722, McGraw-Hill Book Co., New York, 1988.

(26) Dimplefeld, P., Personal Communication, John Deere and Company, Rotary Engine Division, Woodridge, NJ, December, 1989.

(27) Bolz, R. E. and Tuve, G. L.,CRC Handbook of Tables for Applied Engineering Science, 2cnd Edition, CRC Press Inc., Boca Raton, Florida, 1970.

LIST OF SYMBOLS

Symbol	Description
a_r	apex seal crown radius
b	seal base width
C_{A1}, C_{A2}	ancillary loss constants
C_{F1}, C_{F2}, C_{F3}	friction loss constants
c_a	apex seal clearance above the rotor
c_p	specific heat at constant pressure
F_{af}, F_{of}, F_{sf}	apex , oil and side seal friction forces
F_{sa}, F_{so}, F_{ss}	apex, oil and side seal spring forces
$fmep$	friction mean effective pressure
h_a, h_s	apex seal and side seal height
$\overline{h_{hg}}$	average hot gas side heat transfer coefficient

i	enthalpy
k_j	thermal conductivity for material j
L_j	depth of material j
l	seal length
m	mass
$\dot{m}$	mass flow rate
N	engine speed (rpm)
Nu	Nusselt number
P	Pressure
Pr	Prandtl number
$\dot{Q}_{im}$	heat loss rate through intake manifold walls
$\frac{dQ}{d\theta}$	rate of release of fuel energy
$\Re$	gas constant for air
R_o	oil seal radius
Re	Reynolds number
r	trochoid generating radius
T	temperature
t	time
U	overall heat transfer coefficient
V	volume
α	exponent in heat transfer expression
β	coefficient in heat transfer expression
γ	exponent in heat transfer expression
ϵ	eccentricity
θ	crank angle
μ	sliding coefficient of friction
φ	apex seal lean angle
τ	fuel heat release rate decay constant

Subscript	Description
a	apex seal
c	combustion chamber
cc	crank case
$cool$	coolant
epc	exhaust port closing
epo	exhaust port opening
ic	to the intake manifold (from the intercooler)
im	intake manifold
ipc	intake port closing
ipo	intake port opening
max	maximum
o	oil seal
$qmax$	at the time of maximum heat release rate
s	side seal
sp	at the time the spark fires
$wall$	at the trochoid housing wall
1	upstream
2	downstream

LIST OF ABBREVIATIONS

bsfc	brake specific fuel consumption
DISC	direct-injection stratified-charge
fmep	friction mean effective pressure
MIT	Massachusetts Institute of Technology
NASA	National Aeronautics and Space Administration
RCE	rotary combustion engine

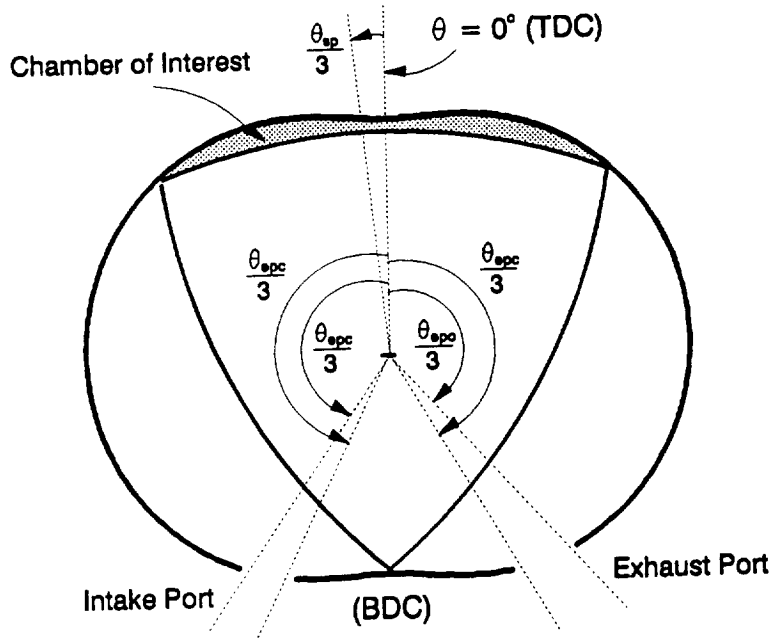

Figure 1: Rotary Engine Schematic

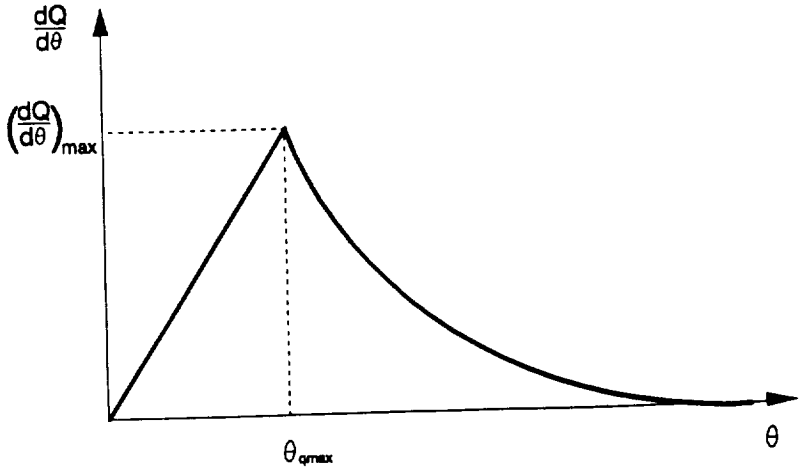

Figure 2: DISC Engine Heat Release Rate

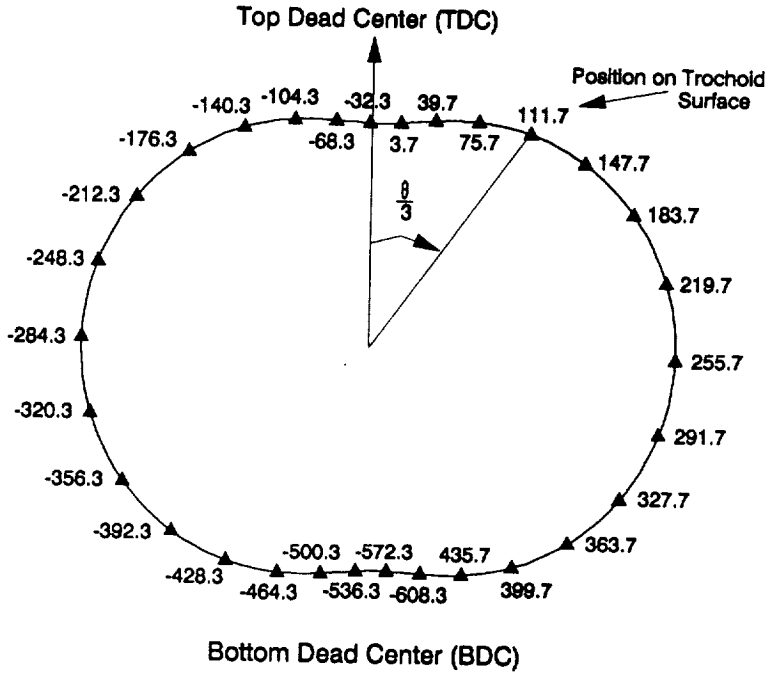

Figure 3: Trochoid Housing Geometry and Crank Angle Definition

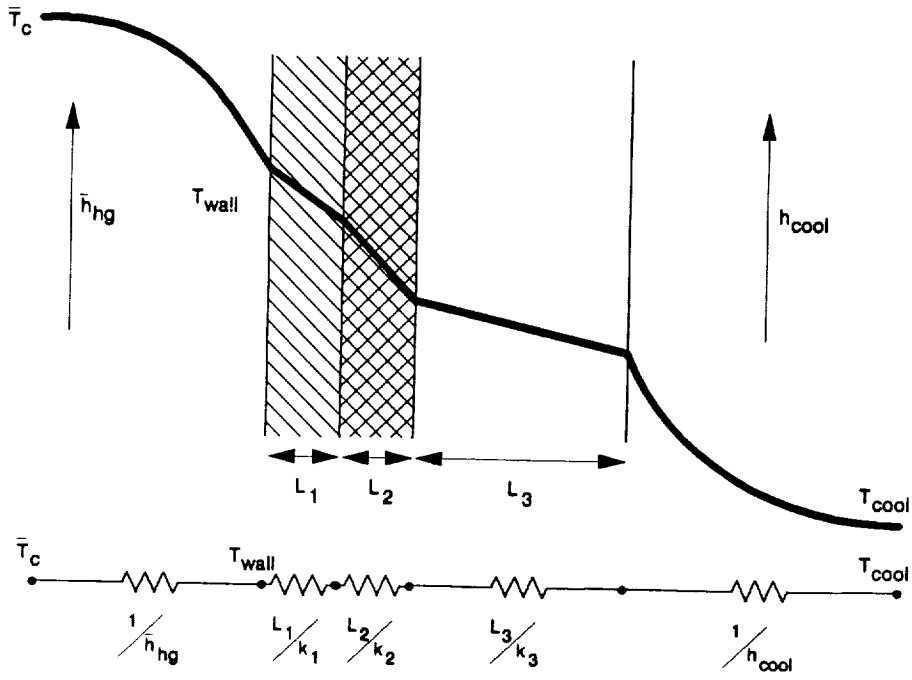

Figure 4: Trochoid Housing Cross Fiction

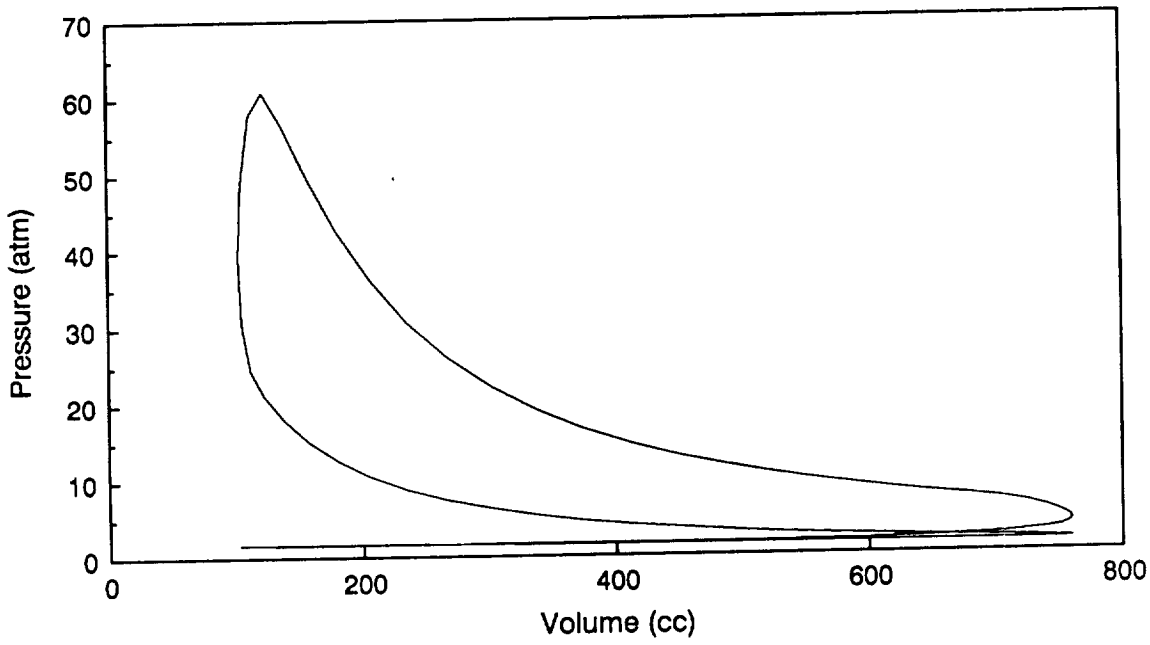

Figure 5: P-V Diagram for DISC RCE, ϕ =0.75, 5500 rpm

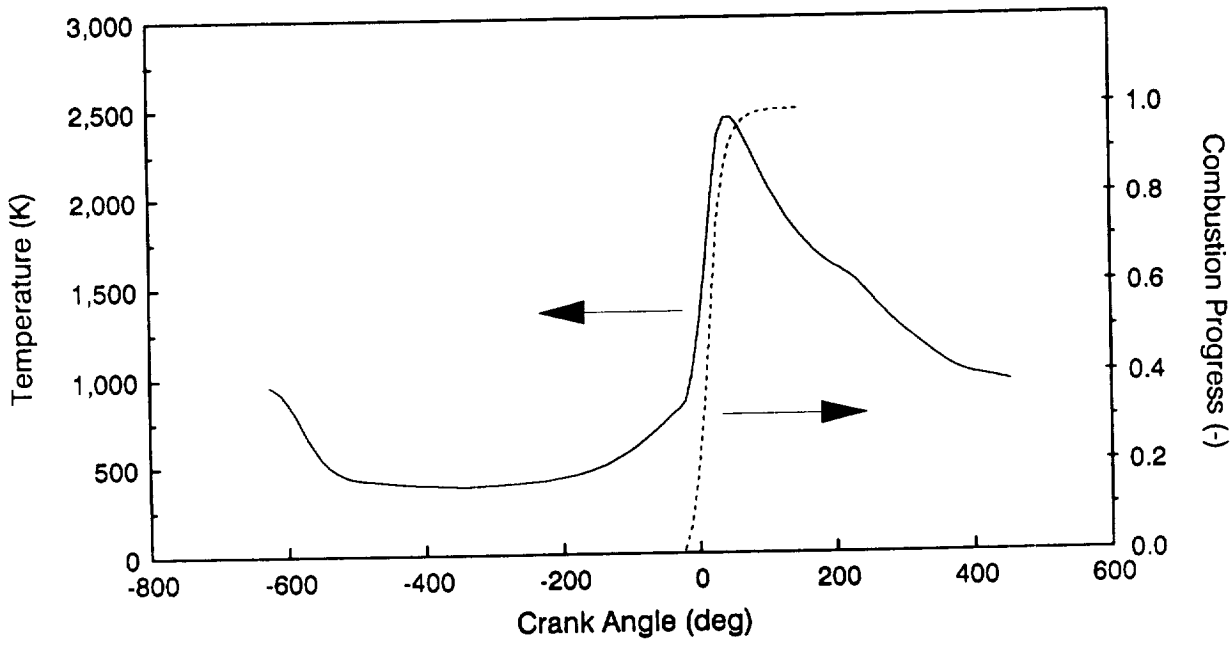

Figure 6: Chamber Temperature and Combustion Progress Histories for a DISC RCE, ϕ = 0.75, 5500 rpm

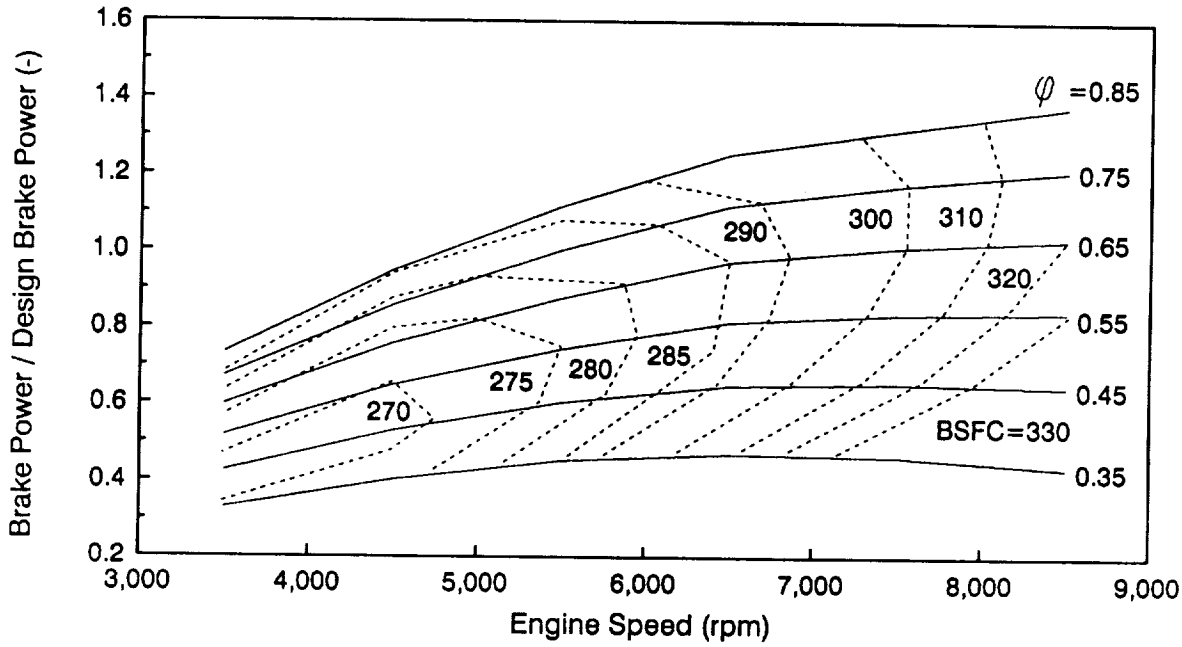

Figure 7: Engine Map for a Single Rotor DISC RCE

Line of Constant φ

Line of Constant BSFC
(BSFC in g/kW-hr)

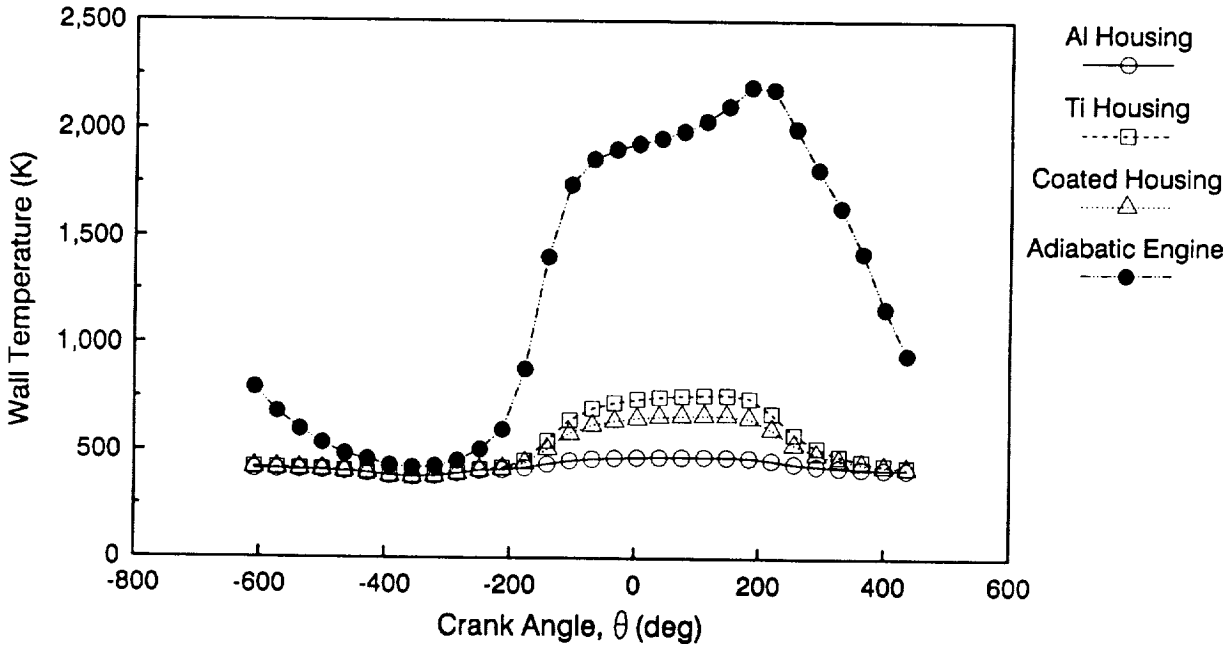

Figure 8: Trochoid Housing Hot Side Wall Temperature for φ=0.75, 5500 rpm and Various Housing Materials

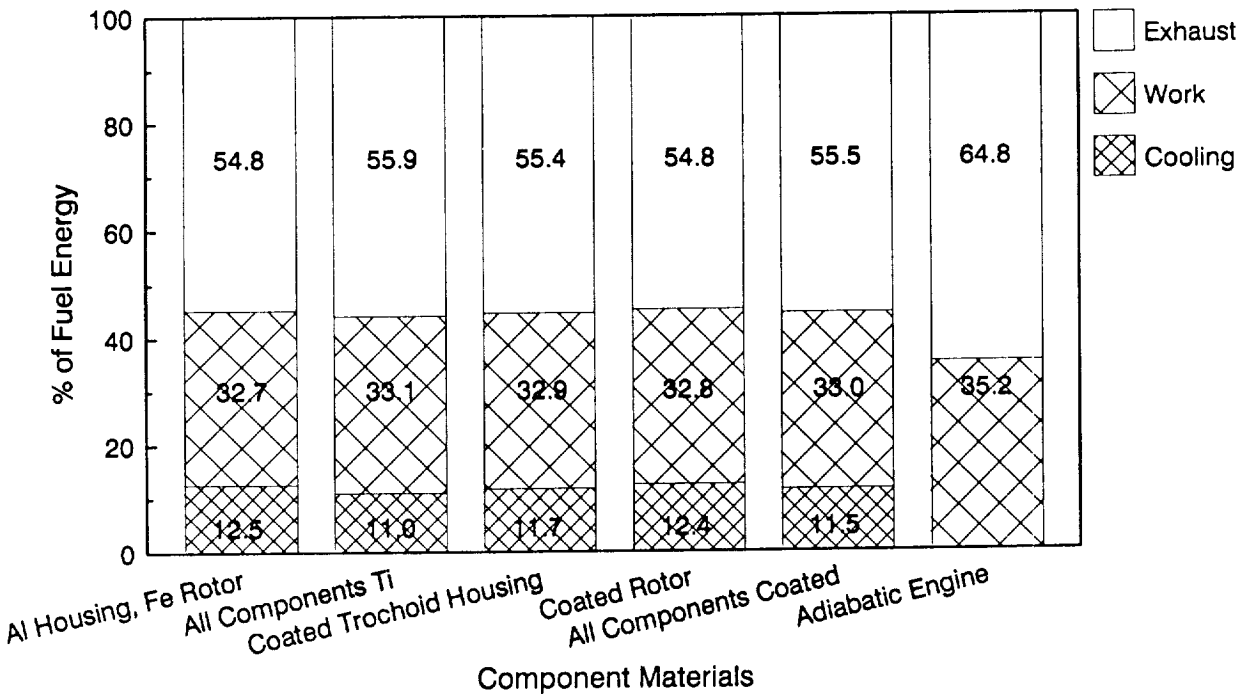

Figure 9: Fuel Energy Diagram for Engines With Various Component Materials, Equivalence Ratio = 0.75, 5500 rpm

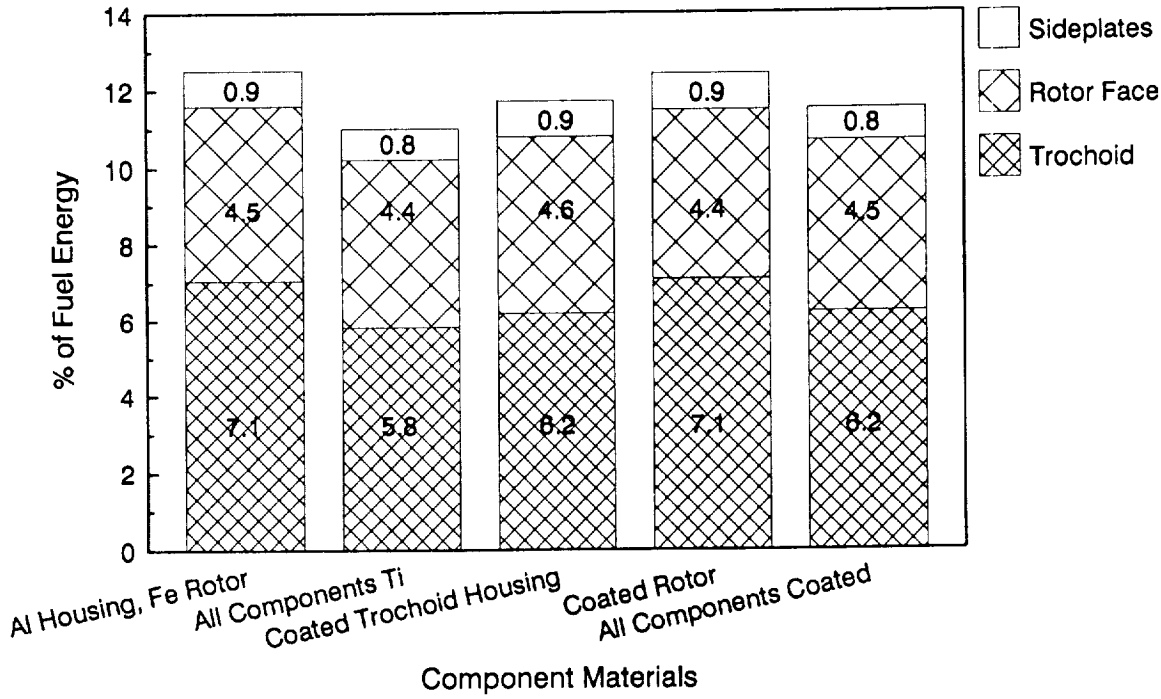

Figure 10: Fuel Energy to Engine Components for Various Component Materials, Equivalence Ratio = 0.75, 5500 rpm

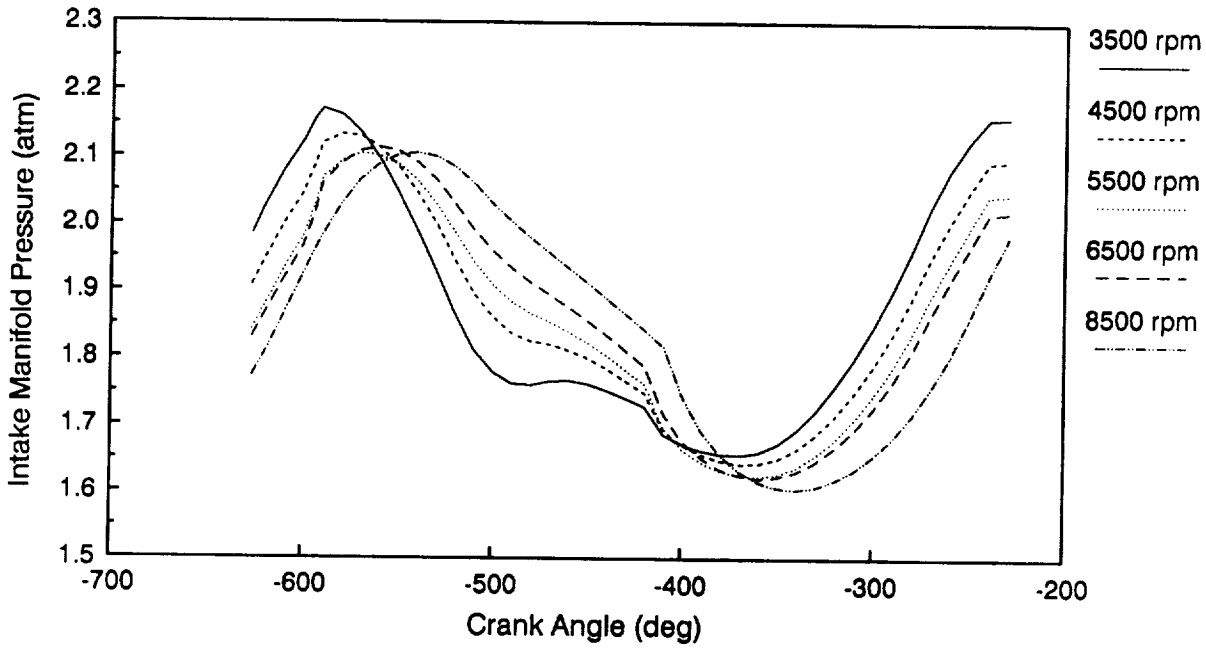

Figure 11: Intake Manifold Pressure Variation During One Intake Event

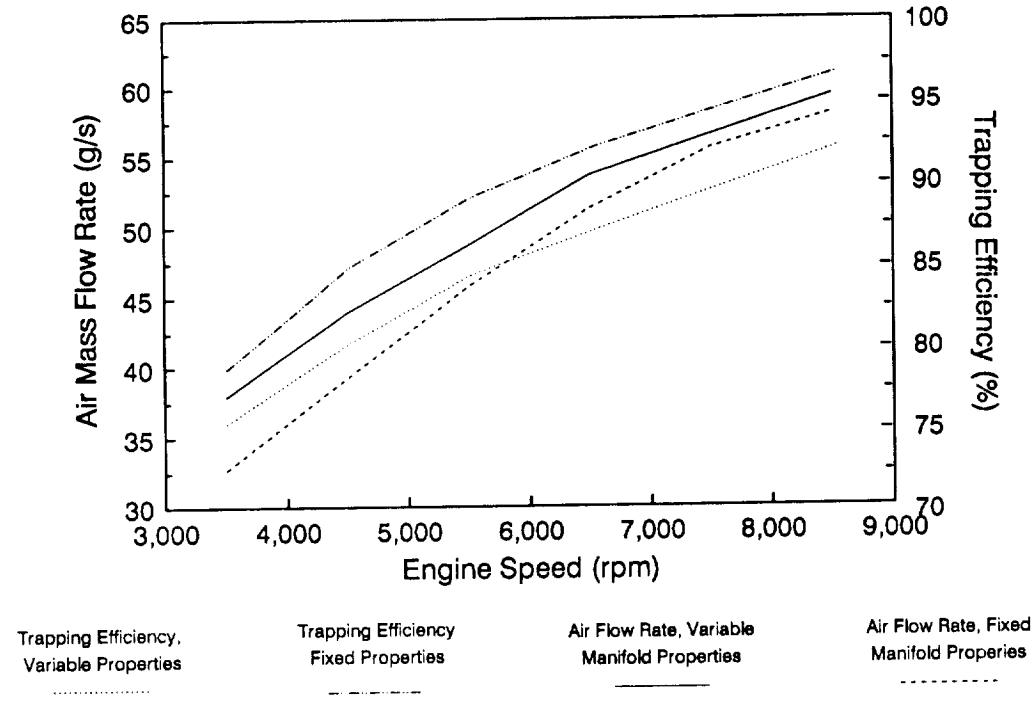

Figure 12: Average Air Mass Flow Rate and Trapping Efficiency for Constant and Variable Intake Manifold Thermodynamic Properties

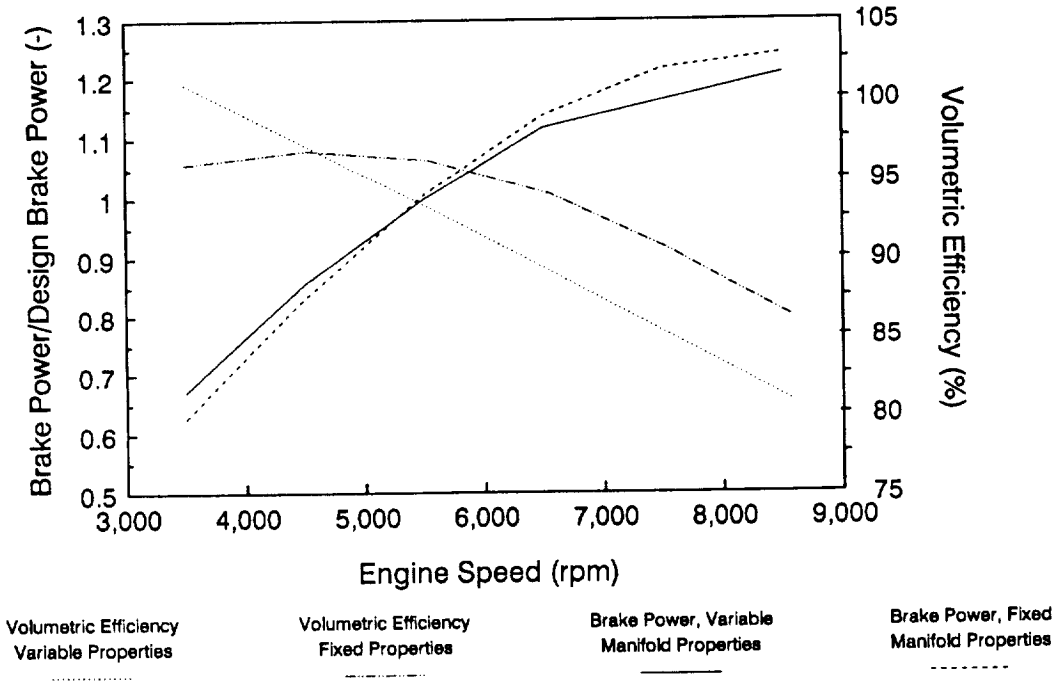

Figure 13: Normalized Brake Power and Volumetric Efficiency for Variable and Constant Intake Manifold Properties

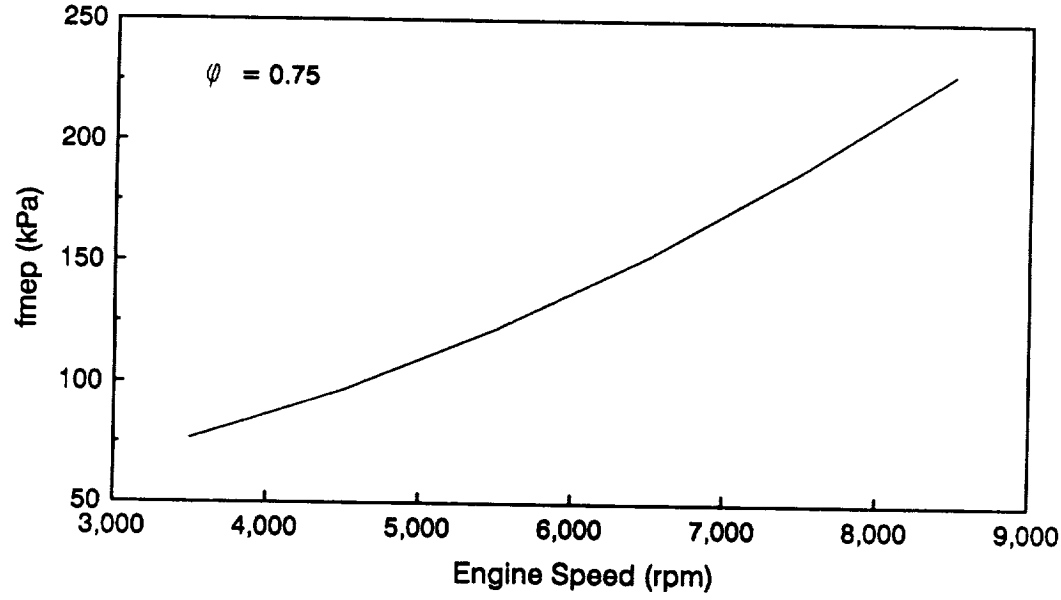

(a) Ancillary Losses

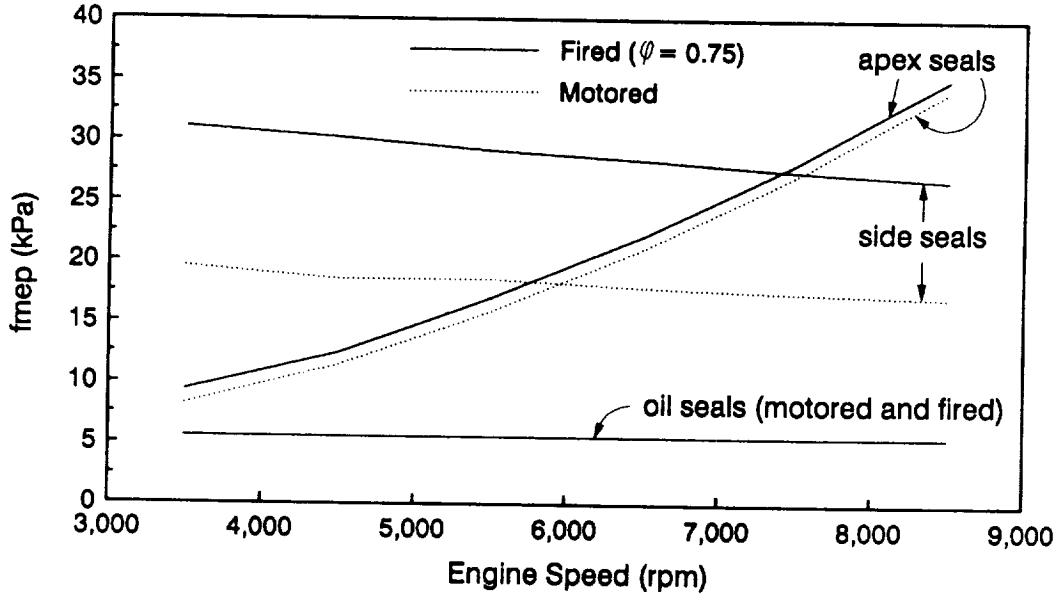

(b) Motored and Fired Seal Losses

Figure 14: Components of Friction Losses

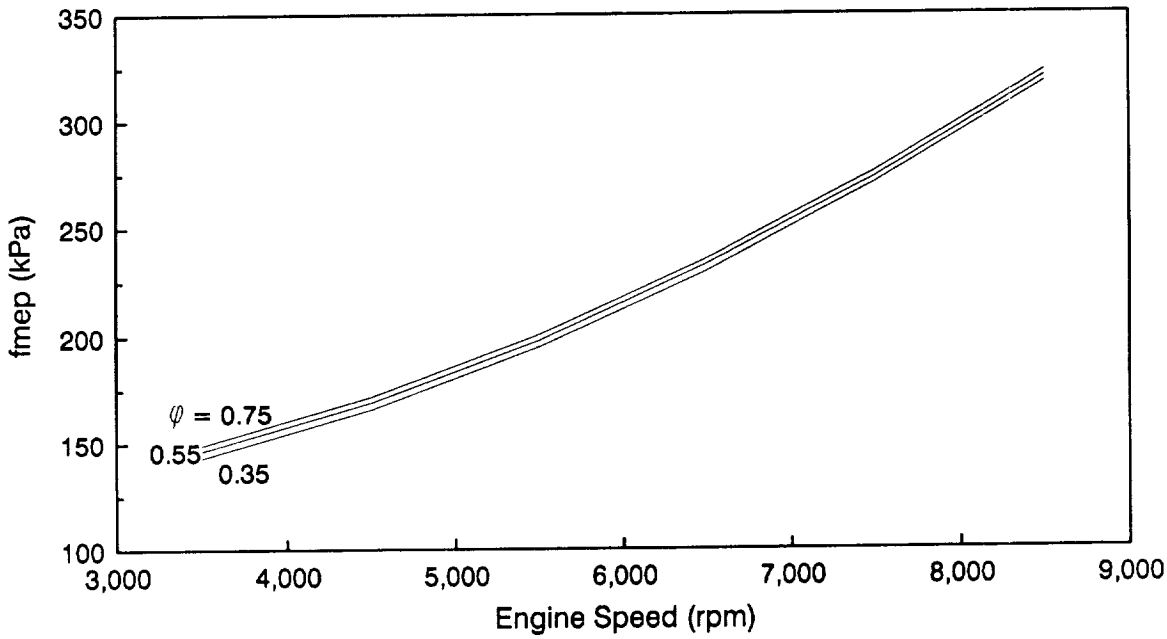

Figure 15: Friction Map

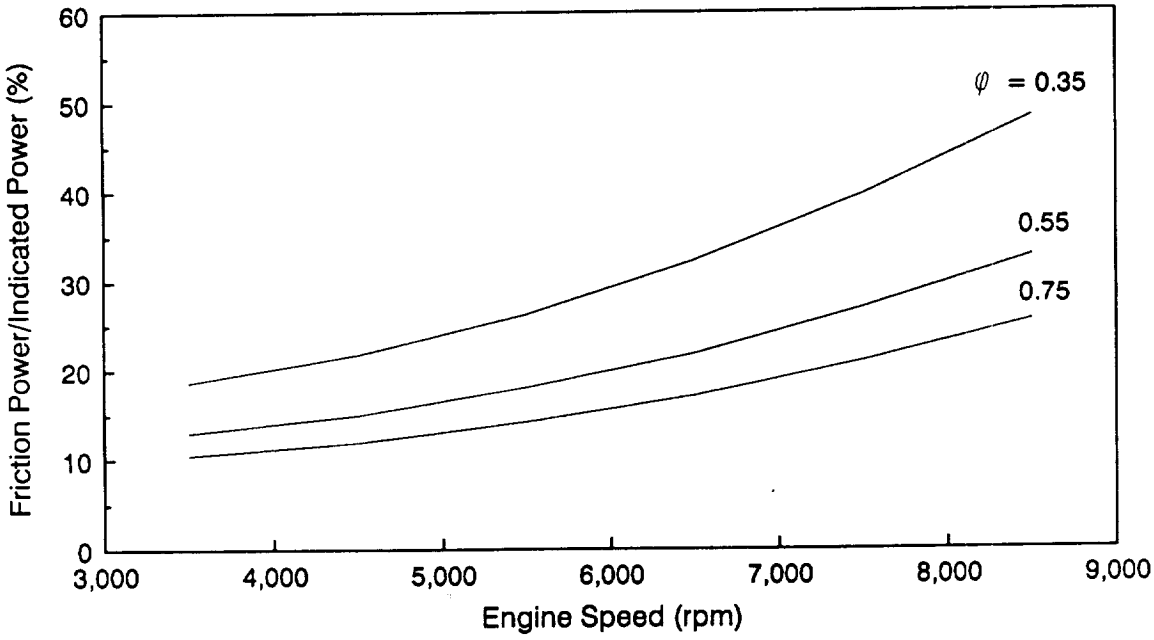

Figure 16: Relative Friction Losses

NASA
National Aeronautics and Space Administration

Report Documentation Page

1. Report No.	2. Government Accession No.	3. Recipient's Catalog No.
NASA TM-103105		

4. Title and Subtitle	5. Report Date
Performance of a Supercharged Direct-Injection Stratified-Charge Rotary Combustion Engine	6. Performing Organization Code

7. Author(s)	8. Performing Organization Report No.
Timothy A. Bartrand and Edward A. Willis	E-5430
	10. Work Unit No. 505-62-11

9. Performing Organization Name and Address	11. Contract or Grant No.
National Aeronautics and Space Administration Lewis Research Center Cleveland, Ohio 44135-3191	13. Type of Report and Period Covered Technical Memorandum

12. Sponsoring Agency Name and Address	14. Sponsoring Agency Code
National Aeronautics and Space Administration Washington, D.C. 20546-0001	

15. Supplementary Notes

Prepared for the Joint Symposium on General Aviation Systems cosponsored by the AIAA and FAA, Ocean City, New Jersey, April 11-12, 1990. Timothy A. Bartrand, Sverdrup Technology, Inc., Lewis Research Center Group, 2001 Aerospace Parkway, Brook Park, Ohio 44142. Edward A. Willis, NASA Lewis Research Center.

16. Abstract

A zero-dimensional thermodynamic performance computer model for direct-injection stratified-charge rotary combustion engines was modified and run for a single rotor supercharged engine. Operating conditions for the computer runs were a single boost pressure and a matrix of speeds, loads and engine materials. A representative engine map is presented showing the predicted range of efficient operation. After discussion of the engine map, a number of engine features are analyzed individually. These features are: heat transfer and the influence insulating materials have on engine performance and exhaust energy; intake manifold pressure oscillations and interactions with the combustion chamber; and performance losses and seal friction. Finally, code running times and convergence data are presented.

17. Key Words (Suggested by Author(s))	18. Distribution Statement
Rotary engine Performance maps Zero-dimensional modelling	Unclassified – Unlimited Subject Category 07

19. Security Classif. (of this report)	20. Security Classif. (of this page)	21. No. of pages	22. Price*
Unclassified	Unclassified	24	A03

*For sale by the National Technical Information Service, Springfield, Virginia 22161